

# Validation Study on Spatially Averaged Two-Fluid Model for Gas–Solid Flows: I. *A Priori* Analysis of Wall Bounded Flows

Simon Schneiderbauer 

Christian-Doppler Laboratory for Multi-scale Modelling of Multiphase Processes, Johannes Kepler University, Altenbergerstr. 69, Linz, Austria

Dept. of Particulate Flow Modelling, Johannes Kepler University, Altenbergerstr. 69, Linz, Austria

DOI 10.1002/aic.16142

Published online March 16, 2018 in Wiley Online Library (wileyonlinelibrary.com)

*In our prior study (Schneiderbauer, AICHE J, 2017;63(8):3544–3562), we presented a spatially averaged two-fluid model, where closure models for the unresolved terms were derived. These closures require constitutive relations for the turbulent kinetic energies (TKEs) of the gas and solids phase as well as for the sub-filter variance of the solids volume fraction (VVF). In this study, we have performed highly resolved TFM simulations of a set of three-dimensional wall dominated periodic channels. An a priori analysis shows that these closures are able to correctly predict the wall profiles of the sub-grid drag modification, the TKEs, the turbulent viscosities and the VVF without requiring special wall corrections. Solely the mixing lengths, which is required by the closures, has to be adapted in the vicinity of wall similar to single-phase turbulence; in particular, the minimum of the filter size and the distance to the wall should be used.*

© 2018 The Authors AICHE Journal published by Wiley Periodicals, Inc. on behalf of American Institute of Chemical Engineers AICHE J, 64: 1591–1605, 2018

*Keywords: cluster induced turbulence, multiphase turbulence, turbulent kinetic energy, kinetic theory based two-fluid model, coarse-grid simulations*

## Introduction

Fluidized beds are widely used in a variety of industrially important processes. One important application of fluidized beds is the circulating fluidized bed (CFB) technology, which implies the return of particles by a looping process. CFBs are widely used for fluid catalytic cracking, circulating fluidized bed combustion (CFBC), and chemical looping combustion. CFBs usually have a riser section, where the solid particles are transported upwards. Inside risers, there are clusters and streamers of particles which are continuously formed and broken.<sup>1–8</sup> They are quite large, with sizes of the order of 10–100 particle diameters.<sup>2,3</sup> They arise from the instability due to the relative motion between gas and particles, as well as from the dissipation of fluctuating energy of particles by both relative motion between particles and viscous damping.<sup>2</sup>

During the last decades the analysis of the hydrodynamics or the efficiency of fluidized beds through numerical simulations has become increasingly common, where the two-fluid

model (TFM) approach has proven to provide fairly good predictions of the hydrodynamics of gas–solid flows.<sup>9</sup> However, due to computational limitations a fully resolved simulation of industrial scale reactors is still unfeasible. It is, therefore, common to use coarse grids to reduce the demand on computational resources, which inevitably neglects small (unresolved) scales.<sup>2</sup> Many sub-grid drag modifications have, therefore, been put forth by academic researchers to account for the effect of small unresolved scales on the resolved meso-scales in this case.

In this context, the heterogeneity based sub-grid models (e.g., EMMS method<sup>10–13</sup> and its derivatives<sup>14–20</sup>) as well as the filtered TFM approach<sup>20–34</sup> should be mentioned. While the heterogeneity based sub-grid models make some specific assumptions about the form of the unresolved clusters and streamers (e.g., spherical clusters of specific solids volume fraction<sup>16,20</sup>), the filtered approaches aim to find appropriate constitutive relations for the unresolved terms appearing due to filtering of the balance equations. Commonly, the filtered sub-grid modifications are deduced from either fine-grid TFM (using grid resolutions of several particle diameters to resolve all relevant flow structures) or well-resolved Euler-Lagrange (EL) simulations,<sup>35–37</sup> which are filtered using filters of different sizes. Different markers such as, solids volume fraction and slip velocity, are then used to classify the sub-filter scale state and averaged to obtain statistics of the filtered quantities. It is apparent that those residual correlations show a considerable dependence on the filter size as well and therefore this dependence is not discussed further.

Additional Supporting Information may be found in the online version of this article.

Correspondence concerning this article should be addressed to S. Schneiderbauer at [simon.schneiderbauer@jku.at](mailto:simon.schneiderbauer@jku.at).

This is an open access article under the terms of the Creative Commons Attribution-NonCommercial License, which permits use, distribution and reproduction in any medium, provided the original work is properly cited and is not used for commercial purposes.

© 2018 The Authors AICHE Journal published by Wiley Periodicals, Inc. on behalf of American Institute of Chemical Engineers

The pioneering work of Igci et al.<sup>22,23</sup> unveils from highly resolved TFM simulations of periodic domains (where the weight of the particles balances the pressure gradient) that the solids volume fraction represents the most important marker determining the sub-filter state. While their one-marker based correlations appear to capture the flow in the core of risers appropriately, their periodic domain simulations do not capture the effect of bounding walls on the cluster behavior.<sup>25</sup> Thus, Igci et al.<sup>24,25</sup> introduce wall corrections accounting for the different behavior of clusters and streamers in the vicinity of bounding walls.<sup>4-6</sup> More recently, several authors presented a second class of filtered models by recognizing that the predictions of the unresolved part of the fluid-solid drag force can be considerably improved by using two markers, these are the filtered solids volume fraction and the filtered slip velocity.<sup>20,26,27</sup> In the case of these two-marker models, Milioli et al.<sup>26</sup> suggest that wall corrections might not be necessary. Zhu et al.<sup>38</sup> studied the requirement of those wall corrections in combination with a two-marker drag modification. In particular, the filtered slip velocity has a negative impact on the filtered drag force in the near-wall regions and hence wall effects may be properly accounted in these two-marker models. However, Zhu et al.<sup>38</sup> could not make a clear statement since they investigated bubbling fluidized beds; but in riser flows there is a clear separation between core and annulus region, where the near-wall flow behavior is quite different from that in the core region of the bed.<sup>39</sup>

Finally, a third class of filtered models employs the concepts of turbulence modeling to derive constitutive relations for unresolved terms.<sup>1,40-44</sup> The development of such turbulence models has a relatively long history in the literature.<sup>2,45-48</sup> On the one hand, Fox and his coworkers<sup>40-43</sup> follow the concept of RANS (Reynolds-averaged Navier Stokes) and on the other hand, Schneiderbauer<sup>1</sup> employed similar to LES (large eddy simulation) a spatial filter to the balance equations. In particular, Capecelatro et al.<sup>41-43,49</sup> derived a Reynolds-stress model (RSM), which is very detailed with respect to the mathematical derivation, but it assumes low particle Reynolds numbers and low particle mass loadings, where the interphase momentum exchange term can be approximated by Stokes' law. Nevertheless, for small particles it provides fairly good estimates of the gas-solid flow near walls.<sup>41</sup> In contrast, the spatially-averaged two-fluid model (SA-TFM) presented in our previous study<sup>1</sup> employs more general representation of the fluid-particle drag force, which is applicable to a wide range of particle Reynolds numbers. Here, the unresolved part of the gas-solid drag force is derived by using a series expansion of the microscopic drag coefficient. The subsequent averaging of this linearized drag force reveals that the unresolved part of the interphase momentum exchange is a function of the turbulent kinetic energies (TKEs) of both, the gas and solid phase, and the variance of the solids volume fraction (VVF). These dependencies are a direct result of the Taylor expansion, which is in contrast to state-of-the-art filtered models solely guessing the most appropriate markers for the sub-filter state. Instead of using functional fits to relate the values of the TKEs and VVF to the local resolved meso-scale state of flow, equations for the TKEs as well as the VVF are derived. This enables the accurate determination of the averaged drag force. However, (i) a detailed *a priori* evaluation of the model predictions near bounding walls and (ii) a comprehensive validation against experimental data is still missing.

In part I of this article, the SA-TFM approach is, therefore, verified in the case of periodic channel flows of Geldart A and B particles by performing an *a priori* analysis of the unresolved terms near bounding walls. In particular, we oppose the predictions of the individual models for the sub-grid drag modification due to unresolved heterogeneous structures (i.e., clusters and streamers), the Reynolds stresses and the VVF-equation to filtered data obtained from highly resolved simulations of three-dimensional periodic channels. Especially, the corrections to the SA-TFM approach near the bounding walls are discussed. In Part II<sup>50</sup> of this article, the SA-TFM approach is applied to the coarse grid simulation of bubbling fluidized beds<sup>51,52</sup> and risers<sup>53</sup> as well as validated against experimental data. Especially, in the latter application the flow behavior is considerably affected by the bounding walls.

## SA-TFM Approach

In Table 1 (Eqs. (1) through (7)) the SA-TFM approach is summarized. The filtered continuity and momentum equations have the same form as the micro-scopic TFM equations (which are summarized in Table A1 in the Appendix) with the phase velocities and other variables now representing filtered  $\bar{\cdot}$  (or Favre averaged,  $\tilde{\cdot}$ ) values.<sup>1,54</sup> The filter operation for a continuous space-time variable  $g(\mathbf{r}, t)$  is given by

$$\bar{g}(\mathbf{x}, t) = \iiint G(\mathbf{x}, \mathbf{r}, \Delta_f) g(\mathbf{r}, t) d\mathbf{r}, \quad (8)$$

with the filter kernel  $G(\mathbf{x}, \mathbf{r}, \Delta_f)$  satisfying  $\iiint G(\mathbf{x}, \mathbf{r}, \Delta_f) d\mathbf{r} = 1$ . Here,  $\Delta_f$  denotes the filter size. Consequently, Favre averages of the  $i$ -th component of the solid- and gas-phase velocities,  $u_i$  and  $v_i$ , read as

$$\begin{aligned} \tilde{u}_i &= \frac{\overline{\phi u_i}}{\bar{\phi}}, \\ \tilde{v}_i &= \frac{\overline{(1-\phi)v_i}}{1-\bar{\phi}}, \end{aligned} \quad (9)$$

where  $\phi$  represents the solids volume fraction. In Eq. 2,  $\rho_q$  ( $q \in \{g, s\}$ ) further denotes the density of either the gas phase  $g$  or the solid phase  $s$ . The filtered momentum equations unveil additional terms representing the unresolved part of the gas-solid drag (denoted by  $H$ ) and Reynolds stress-like contributions,  $R_{s,ik} = -\rho_s \overline{\phi u_i'' u_k''}$  and  $R_{g,ik} = -\rho_g \overline{(1-\phi) v_i'' v_k''}$ , coming from the phase velocity fluctuations,  $u_i'' = u_i - \tilde{u}_i$  and  $v_i'' = v_i - \tilde{v}_i$ .  $H$  is commonly defined as

$$H = 1 - \frac{\sqrt{\overline{\beta(v_i - u_i)} \overline{\beta(v_i - u_i)}}}{\beta \sqrt{(\tilde{v}_i - \tilde{u}_i)(\tilde{v}_i - \tilde{u}_i)}}, \quad (10)$$

where  $\beta$  denotes the microscopic drag coefficient (Eq. A5 in the Appendix) and  $\tilde{\beta}$  is the drag coefficient computed from filtered quantities. Thus, the fractional correction  $H$  is a measure of the subgrid heterogeneity implying a reduction of the resolved drag force  $\tilde{\beta}(\tilde{v}_i - \tilde{u}_i)$ . The Reynolds stresses are approximated by the Boussinesq hypothesis (Eq. 7) and therefore, these are determined by the TKEs of both phases,  $k_g (\equiv \overline{v_i'' v_i''} / 2)$  and  $k_s (\equiv \overline{u_i'' u_i''} / 2)$ , and the turbulent viscosities,  $\mu_{tg}$  and  $\mu_{ts}$ . In the case of sufficiently large filter sizes budget analysis<sup>1,23</sup> show that the filtered kinetic theory stresses  $\overline{\Sigma_{s,ik}^{kc}}$  (Eqs. A3 and A7 in the Appendix) appear negligible compared to the Reynolds-stress like contributions and thus, these are

**Table 1. Summary of SA-TFM Model<sup>1</sup>**

1. Continuity equations of gas and solid phase:

$$\begin{aligned} \frac{\partial(1-\bar{\phi})}{\partial t} + \frac{\partial}{\partial x_k} ((1-\bar{\phi})\tilde{v}_k) &= 0 \\ \frac{\partial\bar{\phi}}{\partial t} + \frac{\partial}{\partial x_k} (\bar{\phi}\tilde{u}_k) &= 0 \end{aligned} \quad (1)$$

2. Momentum equations of gas and solid phase:

$$\begin{aligned} \frac{\partial(1-\bar{\phi})\rho_g\tilde{v}_i}{\partial t} + \frac{\partial}{\partial x_k} ((1-\bar{\phi})\rho_g\tilde{v}_i\tilde{v}_k) &= -(1-\bar{\phi})\frac{\partial\bar{p}}{\partial x_i} + \frac{\partial}{\partial x_k} R_{g,ik} - (1-H)\tilde{\beta}(\tilde{v}_i-\tilde{u}_i) + (1-\bar{\phi})\rho_g g_i, \\ \frac{\partial\bar{\phi}\rho_s\tilde{u}_i}{\partial t} + \frac{\partial}{\partial x_k} (\bar{\phi}\rho_s\tilde{u}_i\tilde{u}_k) &= -\bar{\phi}\frac{\partial\bar{p}}{\partial x_i} + \frac{\partial}{\partial x_k} (R_{s,ik} + \bar{\Sigma}_{s,ik}^{\text{fr}}) + (1-H)\tilde{\beta}(\tilde{v}_i-\tilde{u}_i) + \bar{\phi}\rho_s g_i. \end{aligned} \quad (2)$$

3. Drag correction due to sub-filter heterogenous structures:

$$H = \frac{\left(\frac{\partial\beta}{\partial(1-\bar{\phi})}\right)_{1-\bar{\phi},\tilde{v},\tilde{u}} \sqrt{2\phi\bar{\rho}^2} (\xi_{\phi g} \sqrt{k_g} - \xi_{\phi s} \sqrt{k_s})}{\tilde{\beta} \sqrt{(\tilde{v}_i-\tilde{u}_i)(\tilde{v}_i-\tilde{u}_i)}}. \quad (3)$$

4. TKE of the large-scale velocity fluctuations ( $\tilde{\beta}_\phi = \tilde{\beta}/\bar{\phi}$ ):

$$\begin{aligned} k_g &= \frac{1}{C_{\varepsilon g}^2} \left( -\frac{\bar{\phi}\tilde{\beta}_\phi l_{mg}}{(1-\bar{\phi})\rho_g} + \sqrt{\left(\frac{\bar{\phi}\tilde{\beta}_\phi l_{mg}}{(1-\bar{\phi})\rho_g}\right)^2 + 2\left(l_{mg}^2 \tilde{S}_{g,ij} \tilde{S}_{g,ij} + \frac{\xi_{gs} \bar{\phi} \tilde{\beta}_\phi l_{mg} k_s^{1/2}}{(1-\bar{\phi})\rho_g}\right)} \right)^2, \\ k_s &= \frac{1}{C_{\varepsilon s}^2} \left( -\frac{\tilde{\beta}_\phi l_{ms}}{\rho_s} + \sqrt{\left(\frac{\tilde{\beta}_\phi l_{ms}}{\rho_s}\right)^2 + 2\left(l_{ms}^2 \tilde{S}_{s,ij} \tilde{S}_{s,ij} + \frac{\xi_{gs} \tilde{\beta}_\phi l_{ms} k_g^{1/2}}{\rho_s}\right)} \right)^2. \end{aligned} \quad (4)$$

5. Turbulent viscosity ( $q \in \{g, s\}$ ):

$$\mu_{tq} = \rho_q k_q^{1/2} l_{mq} \quad \text{with} \quad l_{mq} = C_{vq} \Delta r. \quad (5)$$

6. Variance of the sub-filter volume fraction fluctuations:

$$\overline{\phi'^2} = \frac{8}{3} \frac{\xi_{\phi s}^2 k_s \left(\frac{\partial\bar{\phi}}{\partial x_k}\right)^2}{\left(\frac{\partial\tilde{u}_k}{\partial x_k} + C_{\phi s} C_{\varepsilon s} \frac{k_s^{1/2}}{l_{ms}}\right)^2}. \quad (6)$$

7. Reynolds-stress like contributions:

$$\begin{aligned} R_{g,ik} &= -\frac{2}{3} (1-\bar{\phi})\rho_g k_g + 2(1-\bar{\phi})\mu_{tg} \tilde{S}_{g,ik}, \\ R_{s,ik} &= -\frac{2}{3} \bar{\phi}\rho_s k_s + 2\bar{\phi}\mu_{ts} \tilde{S}_{s,ik}. \end{aligned} \quad (7)$$

8. Model constants:

Constant	Value	Constant	Value	Constant	Value	Constant	Value	Constant	Value
$\xi_{gs}$	0.8	$\xi_{\phi s}$	0.1	$\xi_{\phi g}$	$-0.5(1-\bar{\phi})$	$C_{\varepsilon g}$	0.7	$C_{\varepsilon s}$	1
$C_{vg}$	0.4	$C_{vs}$	0.25	$C_{\phi g}$	0.4	$C_{\phi s}$	0.25		

not considered in this study. However, in the dense flow regime (i.e.,  $\phi > 0.5$ ) the contribution stemming from the filtered frictional stresses  $\bar{\Sigma}_{s,ik}^{\text{fr}}$  appears non-negligible even though we employ large filter sizes.<sup>20</sup> It has to be stressed that in a first step we approximate the filtered frictional stresses by

its microscopic counterpart,  $\Sigma_{s,ik}^{\text{fr}}$  (Eqs. A7, A14, and A15 in the Appendix), evaluated by using deviatoric part of the filtered rate-of-deformation tensor,  $\tilde{S}_{s,ik}$ . Closure models for the filtered frictional stress models will be discussed in future publications.

**Table 2. Material Properties and Operating Conditions for the Fine Grid Simulations<sup>16,20</sup>**

Property	Case 1	Case2
$\phi^{\max}$		0.6
$\phi^{\text{fr}}$		0.4
$\langle \phi \rangle / \phi^{\max}$		0.25
$\mu_i^{\text{st}}$	0.38 (=tan(20.8°))	
$d_s$	75 $\mu\text{m}$	150 $\mu\text{m}$
$\rho_s$	1780 $\text{kg m}^{-3}$	2500 $\text{kg m}^{-3}$
$\rho_g$	1.224 $\text{kg m}^{-3}$	1.224 $\text{kg m}^{-3}$
$\mu_g$	$1.78 \cdot 10^{-5} \text{ kg m}^{-1}\text{s}^{-1}$	$1.78 \cdot 10^{-5} \text{ kg m}^{-1}\text{s}^{-1}$
$u_t$	0.26 $\text{m s}^{-1}$	0.96 $\text{m s}^{-1}$
$\text{Fr}_p$	92	626
$\mathbb{L}_{\text{ch}}/d_s$	4.5	8.55
$W_g$	5 $\text{m s}^{-1}$	
$\hat{\Delta}_g$	1	1
$\hat{\Delta}_d$	256×64×512	

Note these properties correspond to Geldart group A and B type particles ( $\phi^{\max}$ : solids volume fraction at maximum packing conditions;  $\phi^{\text{fr}}$  threshold solids volume fraction, where the frictional stress become active;  $\langle \phi \rangle$ : domain averaged solids volume fraction;  $\mu_i^{\text{st}}$ : static coefficient of internal friction;  $d_s$ : particle diameter;  $\rho_s$ : particle density;  $\rho_g$ : gas-phase density;  $\mu_g$ : gas-phase dynamic viscosity;  $W_g$ : superficial gas velocity;  $u_t$ : terminal settling velocity;  $\text{Fr}_p$ : particle Froude number;  $\hat{\Delta}_g$ : dimensionless grid spacing;  $\hat{\Delta}_d$ : dimensionless domain size, which is given by  $\hat{\Delta}_d=2W \times D \times \mathcal{H}$ ).

Constitutive relations for the unclosed terms, these are  $H$ ,  $k_g$ ,  $k_s$ ,  $\mu_{ig}$ , and  $\mu_{ig}$ , are given in Table 1 as well. Here,  $H$  is derived from averaging the microscopic drag force, where the microscopic drag coefficient is approximated by a Taylor series expansion.<sup>1</sup> The constitutive model for the drag correction clearly unveils that the meso-scale drag (evaluated from filtered quantities) is mainly reduced in regions of a considerable VVF  $\overline{\phi^2}$  ( $=\overline{\phi^2}-\overline{\phi}^2$ ),<sup>36,55</sup> as well as in regions showing a high degree of sub-filter velocity fluctuations. Thus, transport equations for  $k_g$ ,  $k_s$ , and  $\overline{\phi^2}$  were derived.<sup>1</sup> In moderately dilute and moderately dense gas–solid flows (i.e., solid volume fractions between 0.1 and 50%)<sup>40</sup> it is plausible to neglect the transport of the turbulent velocity fluctuations and to assume that turbulence is determined by local production and dissipation.<sup>42</sup> We will show later that employing this simplification reveals good agreement with the fine grid data. In contrast to single phase turbulence an additional source of turbulent production appears in the equations for  $k_g$  and  $k_s$ , which is stemming from the interfacial work due to the gas–solid drag. This additional source of turbulence was also recently described by Fox,<sup>40</sup> who referred this phenomenon to as cluster induced turbulence (CIT). Interestingly, the constitutive model for  $\overline{\phi^2}$  (which can be derived from the microscopic continuity equation) is mostly dependent on the kinetic energy of the solids velocity fluctuations and the gradient of the solids volume fraction. Thus, velocity fluctuations as well as gradients in the particle concentration enhance the sub-filter heterogeneity of the granular system. Physically, this is mostly pronounced at the borders of resolved clusters and bubbles.<sup>1</sup> Our previous study clearly shows that the turbulent viscosities can be approximated by a mixing length model (Eq. 5), that is

$$\mu_{iq} = \rho_q k_q^{1/2} l_{mq},$$

where the mixing length  $l_{mq} = C_{vq} \Delta_f$  is determined by the filter width  $\Delta_f$ . Finally, in contrast to state-of-the-art filtered closures the present constitutive relations solely depend on nine model constants,<sup>1</sup> which appear to apply to a wide range of particle properties (size and density).

## Case Description

To investigate the heterogenous sub-filter structures near bounding walls we performed fine grid simulations following previous work.<sup>20,26,27</sup> Thereby, we employed a kinetic-theory based TFM,<sup>9,56</sup> which is discussed in the appendix (Table A1 in the Appendix), to three-dimensional periodic channels<sup>29,44</sup> of width  $2W$ , depth  $D$ , and height  $\mathcal{H}$  (Table 2). Here, we applied a fixed superficial gas velocity, which was obtained by adjusting the gas-phase pressure gradient using a PID (proportional-integral-derivative) controller. It has to be further noted that only the first horizontal dimension is constrained by walls, while the second horizontal and the vertical dimensions are considered periodic (compare with Figure 1 in our previous study<sup>44</sup>). In dense regions, i.e., where the solids volume fraction is close to the maximum packing conditions and the inter-particle forces are dominated by long enduring multiple frictional contacts, the solid stress was closed by using a inertial number dependent rheology (Eqs. A14 and A15 in the Appendix).<sup>9,57</sup> The wall shear stresses and the flux of fluctuation energy at the bounding walls were modeled by partial-slip boundary conditions proposed recently.<sup>58</sup> These boundary conditions incorporate sliding and non-sliding collisions.<sup>59–65</sup> Recently, it was shown that these boundary conditions apply well to fluidized beds,<sup>9</sup> moving beds,<sup>9</sup> and riser flows.<sup>66</sup> The main physical properties relevant for this study are summarized in Table 2.

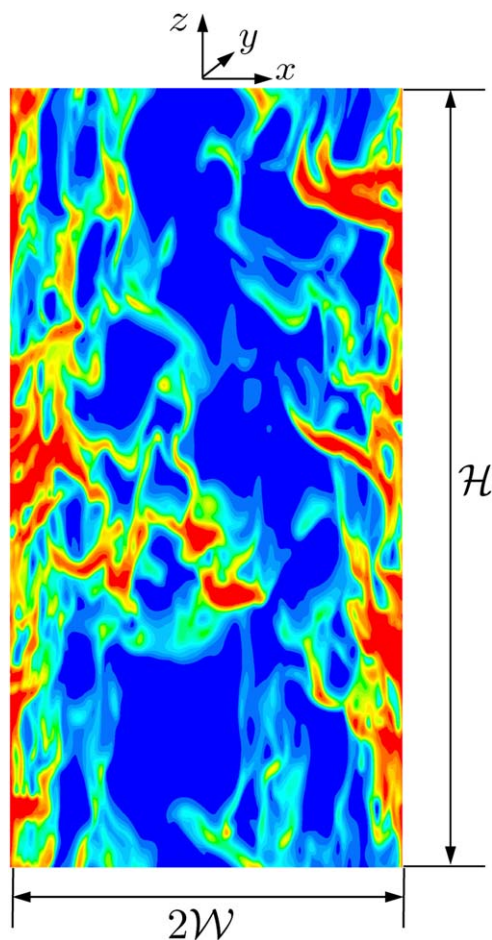


**Figure 1. Snapshot of particle clusters in a three-dimensional periodic channel for Case 2.**

[Color figure can be viewed at [wileyonlinelibrary.com](http://wileyonlinelibrary.com).]

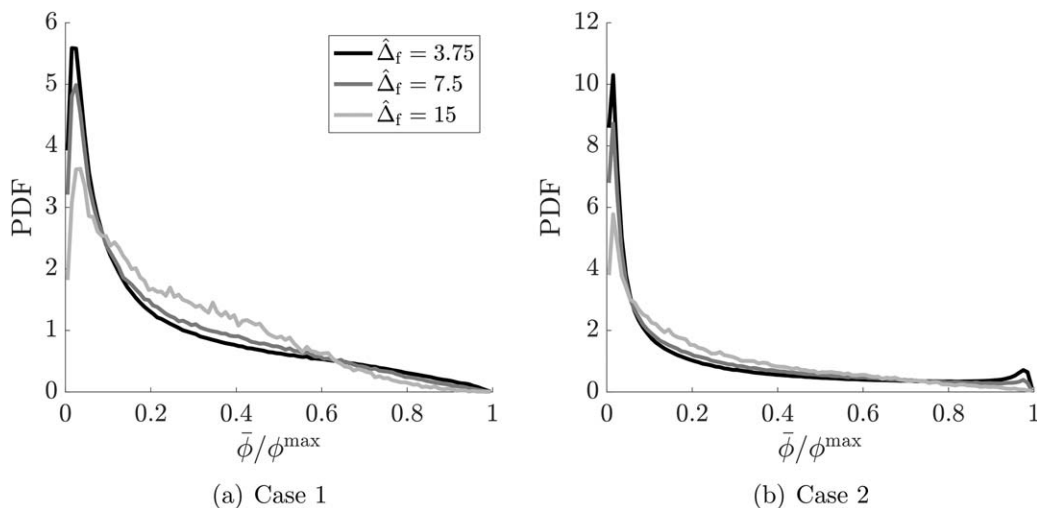


**Figure 2.** PDFs (probability density function) of the normalized filtered solids volume fraction  $\bar{\phi}/\phi^{\max}$  for different dimensionless filter sizes,  $\hat{\Delta}_f = \Delta_f/l_{ch}$  and a domain averaged volume fraction of  $\langle \phi \rangle / \phi^{\max} = 0.25$ .

The convective terms in the momentum equations (Eqs. A2 and A3 in the Appendix) are discretized by using a second-order upwind scheme. The derivatives appearing in the viscous terms are computed by a least squares method, and the pressure-velocity coupling is achieved by the SIMPLE algorithm, whereas the face pressures are computed as the average of the pressure values in the adjacent cells (linear interpolation).

The simulations were started from a slightly nonuniform settled state to expedite the development of inhomogeneous flow structures. After an initial transient period the system reached a statistical steady state with persistent temporally and spatially distributed clusters (compare with Figure 1). Following previous work,<sup>1,26,27</sup> snapshots of the flow field were collected at various times after the initialization phase. These computational data were then filtered using filters of different sizes, where we employed a box filter in this study defined as

$$G(\mathbf{x}, \mathbf{r}, \Delta_f) = \begin{cases} \frac{1}{\Delta_f^3}, & \text{if } \mathbf{r} - \mathbf{x} \in [-\Delta_f/2, \Delta_f/2]^3 \\ 0, & \text{otherwise} \end{cases} \quad (11)$$

Finally, it has to be emphasized that the grid spacing was set fine enough to resolve all relevant heterogeneous structures.<sup>67–74</sup> For example, Fullmer and Hrenya<sup>67</sup> obtain mesh-convergence of TFM using a grid spacing of about  $4.4d_s$  in the case of moderately-dense gas–solid flows of Geldart A type particles, while the simulations of Uddin and Coronella<sup>69</sup> unveil that much larger grid spacings can be used for Geldart type B particles. Table 2 shows that we used a grid spacing of  $4.5d_s$  and  $8.55d_s$  for the Geldart type A and B particles, respectively. These values clearly meet the above mesh-convergence requirements. Note that we made the filter size and grid spacing dimensionless by using the characteristic length scale,<sup>20,37,75</sup>

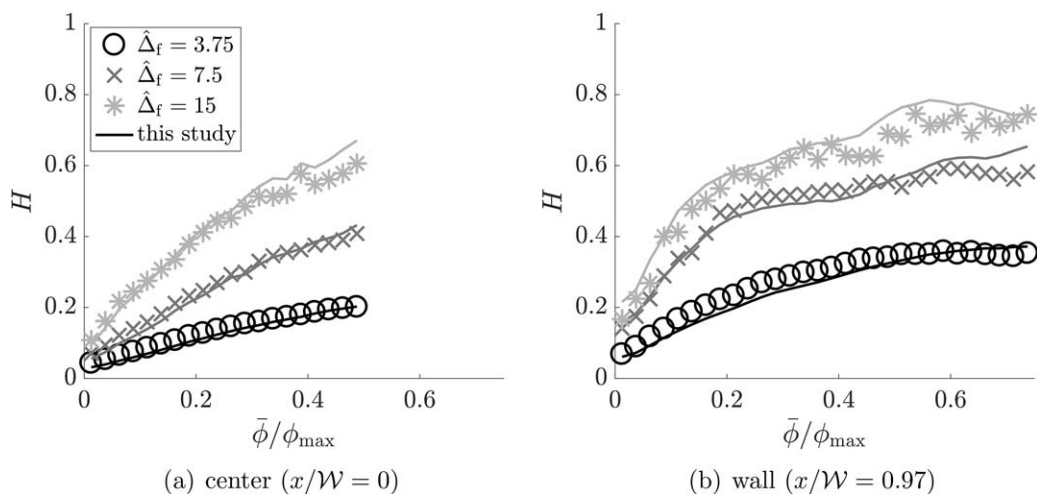


**Figure 3.** Fractional correction,  $H$ , as a function of the normalized filtered solids volume fraction,  $\bar{\phi}/\phi^{\max}$ , for Case 1 in (a) the center of the channel and (b) near the walls.

The symbols correspond to measurements from the fine grid simulations and the solid lines denote the predictions employing Eq. 3.

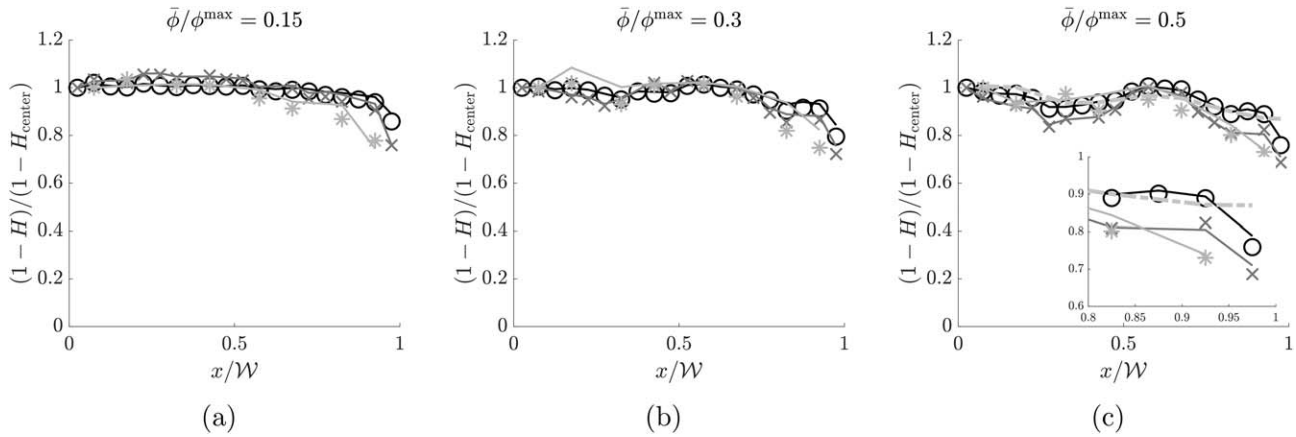


**Figure 4.** Normalized fractional correction,  $(1-H)/(1-H_{\text{center}})$ , as a function of the normalized horizontal coordinate,  $x/W$ , for Case 1 for different normalized solids volume fractions,  $\bar{\phi}/\phi^{\text{max}}$ .

The dashed-dotted line in (c) corresponds to the drag modification proposed by Sarkar et al.<sup>27</sup> for  $\hat{\Delta}_f=15$ . The remaining symbols and lines have the same meaning as in Figure 3.

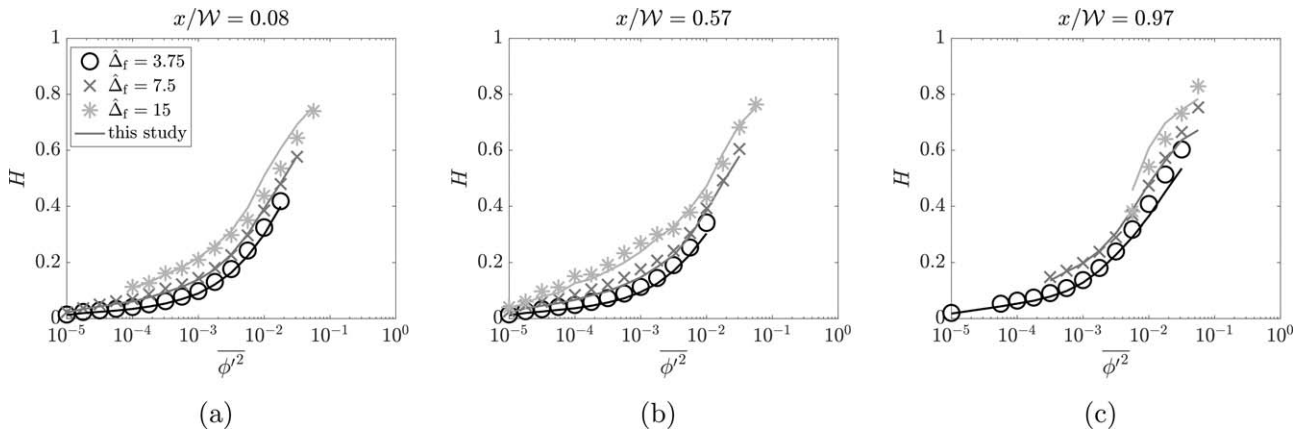


**Figure 5.** Fractional correction,  $H$ , as a function of the variance of the solids volume fraction,  $\bar{\phi}^2$ , for Case 1 at different locations in the vertical channel,  $x/W$ .

The symbols and lines have the same meaning as in Figure 3.

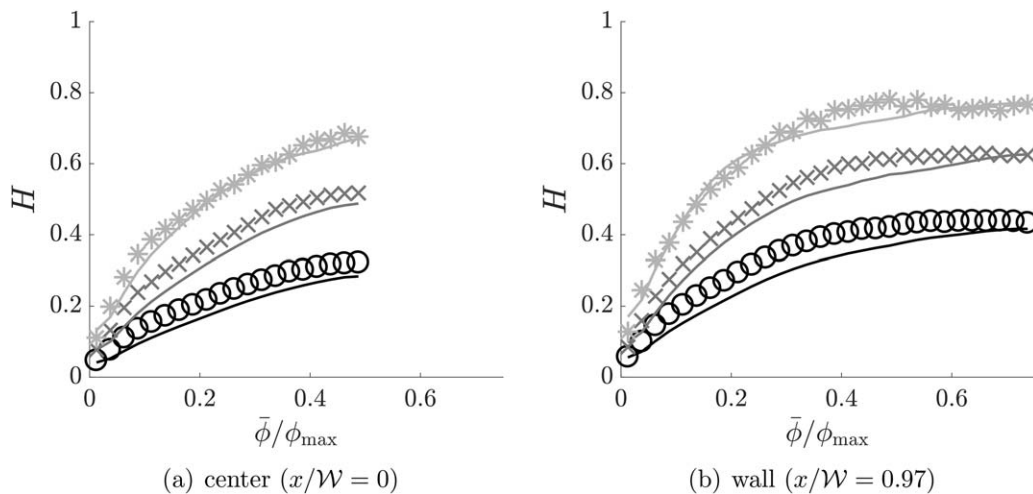


**Figure 6.** Fractional correction,  $H$ , as a function of the normalized filtered solids volume fraction,  $\bar{\phi}/\phi^{\text{max}}$ , for Case 2 in (a) the center of the channel and (b) near the walls.

The symbols and lines have the same meaning as in Figure 3.

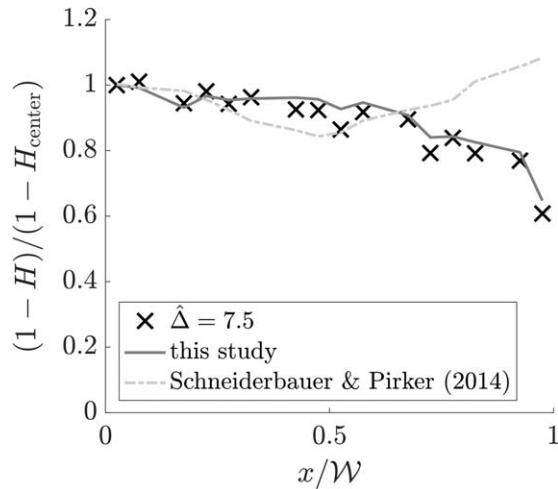


**Figure 7.** Normalized fractional correction,  $(1-H)/(1-H_{\text{center}})$ , as a function of the normalized horizontal coordinate,  $x/W$ , for  $\bar{\phi}/\phi^{\text{max}}=0.5$  and  $\Delta=7.5$  (Case 2).

The dashed corresponds to the drag modification proposed by Schneiderbauer and Pirker.<sup>15</sup> The remaining symbols and lines have the same meaning as in Figure 3.

$$\mathbb{L}_{\text{ch}} = \frac{u_t^2}{g} \text{Fr}^{-2/3}, \quad (12)$$

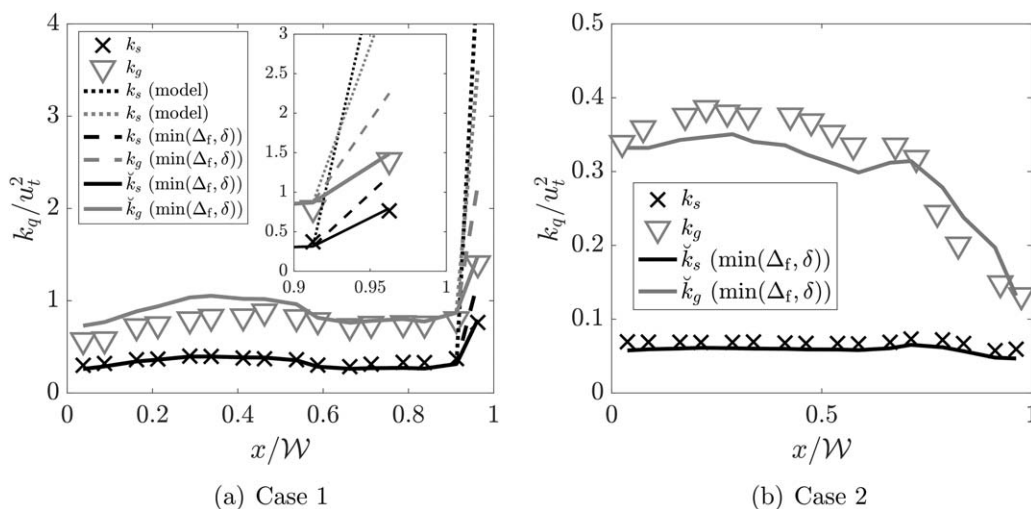
where  $u_t$  denotes the terminal settling velocity,  $g$  the standard acceleration due to gravity, and  $\text{Fr}=u_t^2/(d_s g)$  the particle-based Froude number.

### A Priori Analysis of Gas–Solid Flows Near Walls

In order to elucidate the applicability of the SA-TFM approach to different gas–particle flow regimes (i.e., dilute, dense), Figure 2 presents the PDFs (probability density function) of the filtered solids volume fraction for different filter sizes obtained from both fine grid simulations. The figure discloses that even though the domain averaged volume fraction is  $\langle \phi \rangle / \langle \phi^{\text{max}} \rangle = 0.25$ , the PDFs show their maxima at

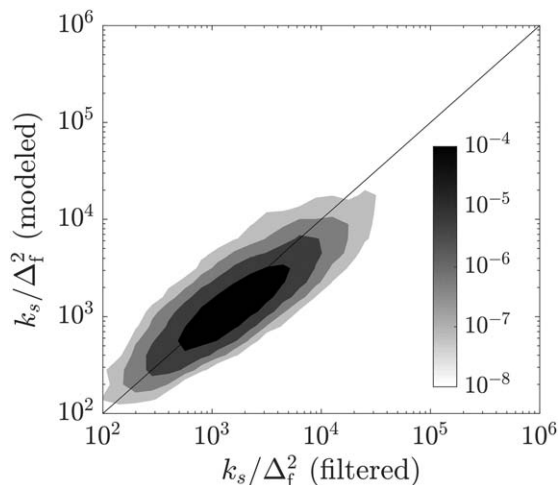
$\langle \phi \rangle / \langle \phi^{\text{max}} \rangle = 0.025$  and  $\langle \phi \rangle / \langle \phi^{\text{max}} \rangle = 0.015$  for the Geldart type A and B particles, respectively. This, in turn, implies that most of the filter samples represent moderately dilute (i.e.,  $0.001 \leq \phi \leq 0.05$ ) to moderately dense (i.e.,  $0.05 \leq \phi \leq 0.5$ ) conditions. In particular, here particle–particle collisions are the dominant contribution to the microscopic particle stress tensor  $\Sigma_{s,ik} = \Sigma_{s,ik}^{\text{kc}} + \Sigma_{s,ik}^{\text{fr}}$  (Eq. A16 in the Appendix). Collisional particle flows can exhibit particle-phase turbulence (e.g., due to mean shear) even though in the absence of the fluid phase and the momentum coupling between the two phases can lead to a new source of turbulence, which is stemming from the interfacial work (i.e., drag).<sup>1</sup> Here,  $R_s$  is much larger than  $\overline{\Sigma_{s,ik}^{\text{kc}}}$ . In contrast, in dilute gas–particle flows ( $\phi \leq 0.001$ ) the kinetic-streaming contribution to the particle-phase stress tensor gets significant compared to the turbulent stresses.<sup>40</sup> This, in turn, implies that  $\overline{\Sigma_{s,ik}^{\text{kc}}}$  has to be considered in the momentum Eq. 2 in dilute gas–particle flows, which would require a closure model for  $\overline{\Sigma_{s,ik}^{\text{kc}}}$ . In very dense gas–solid flows (i.e., close to maximum packing conditions;  $\phi \geq 0.5$ ), frictional contacts get dominant<sup>9</sup>; these can be considered as considerably source of turbulence dissipation and consequently turbulent fluctuations become insignificant under these conditions.<sup>1</sup> However, the figure shows that the number of filter samples in the dilute and dense regimes is very low for both cases and therefore, we solely consider moderately dilute to moderately dense conditions in Figures 3–16. These figures will clearly show that the SA-TFM approach is applicable to these flow regimes. It has to be further stressed that the SA-TFM approach can be further extended to the dense regime if an appropriate frictional stress model is applied (compare with Eq. 2). This will be shown in part II of this article.

Figure 3 shows the results of the *a priori* analysis for the fractional correction  $H$  (Eq. 3) for Case 1 (Geldart A type particles). The figure clearly shows that Eq. 3 correctly predicts the reduction of the drag force due to the formation of heterogeneous structures in the channel center (Figure 3a) as well as near the channel walls (Figure 3b). Furthermore, the fine grid simulations reveal that  $H$  gets larger with increasing normalized filter size ( $\hat{\Delta}_f = \Delta_f / \mathbb{L}_{\text{ch}}$ ), which is generally accepted in the literature.<sup>20,22,23,26–29</sup> Remarkably, Eq. 3 correctly



**Figure 8.** Normalized large-scale TKEs of the gas and solid phase,  $k_q/u_t^2$ , as a function of the normalized horizontal coordinate,  $x/W$ , for  $\hat{\Delta}_f=7.5$ .

The symbols correspond to measurements from the fine grid simulations and the solid lines denote the predictions employing Eq. 4 with  $I_{mq} = C_{vq} \min(\Delta_f, \delta)$ .



**Figure 9. Parity plot comparing  $k_s/\Delta_f^2$  obtained from (i) filtering Case 1 and (ii) Eq. 4.**

The filter size is  $\hat{\Delta}_f=15$ . The colorbar corresponds to the probability of occurrence of different pairs of measured and modeled TKEs.

estimates the filter size dependence of the drag reduction, even though there is no explicit dependence on the filter size in the closure model. In particular, the filter size dependence is hidden in the variances  $\overline{\phi^2}$ ,  $k_g$ , and  $k_s$ ; their filter size dependencies will be discussed later. Comparing Figures 3a, b further

suggests that the heterogeneous structures are more pronounced near the wall, which manifest in a higher drag reduction at equal filter size and equal filtered solids volume fractions. This has also been observed by Ipci and Sundaresan.<sup>23</sup> They rationalized this increase of the drag reduction near walls as follows: Fluctuations of the solids velocity and the solids volume fraction will be dampened in the vicinity of solid boundaries. As the fluctuations associated with the meso-scale structures contribute to breakup of clusters, diminished fluctuations near the boundaries result in larger clusters and hence lower drag coefficient.

In Figure 4 we delineate the behavior of  $H$  for Case 1 as a function of the normalized horizontal coordinate  $x/\mathcal{W}$ , that is the distance from the channel center normalized by the half of the channel width,  $\mathcal{W}$ . It has to be noted that in Figure 4 the fractional correction is normalized by its value at the center,  $H_{\text{center}}$ . Depending on the filter size the modification of the resolved drag force,  $1-H$ , is up to 30% smaller than observed in the core of the channel. Note that our results cannot be compared directly with the findings of Ipci and Sundaresan,<sup>23</sup> since we solely investigate the radial dependence of  $H$  instead of the radial dependence of the total filtered drag coefficient. In addition, we employ a three-dimensional vertical channel flow instead of studying a two-dimensional riser. However, our results clearly confirm that the drag modification at the channel wall is considerably different compared to the center yielding a more distinct reduction near the wall. For a more detailed discussion on the impact of different parameters, such as channel width, the reader is referred to Ipci and Sundaresan.<sup>23</sup>

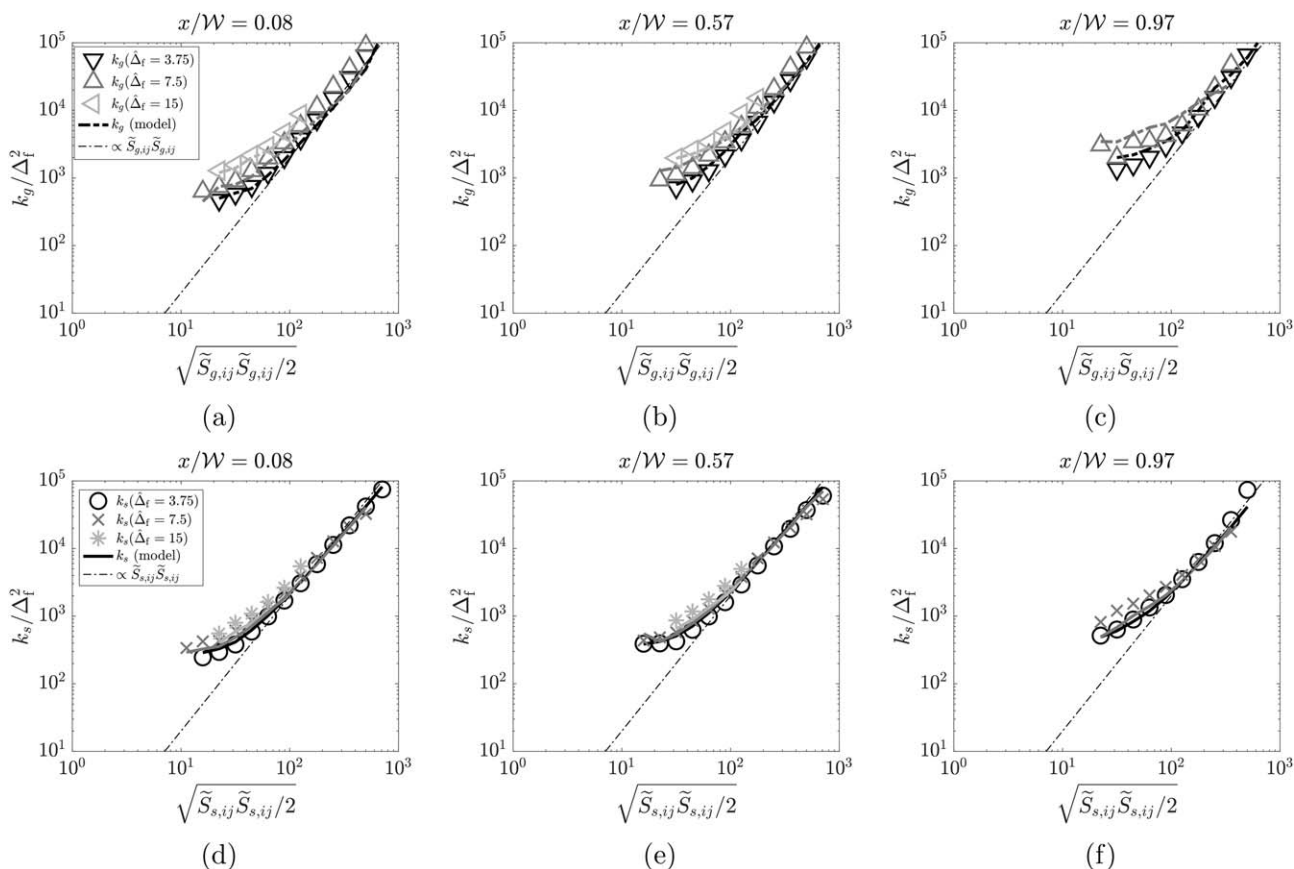


**Figure 10. Normalized large-scale TKEs of the gas and solid phase,  $k_g/\Delta_f^2$  and  $k_s/\Delta_f^2$ , as a function of the scalar shear rates,  $\sqrt{\tilde{S}_{g,ij}}\tilde{S}_{g,ij}/2$  and  $\sqrt{\tilde{S}_{s,ij}}\tilde{S}_{s,ij}/2$ , at different locations  $x/\mathcal{W}$  for Case 1.**

The symbols indicate the fine grid data, while the solid and dashed lines correspond to Eq. 4.

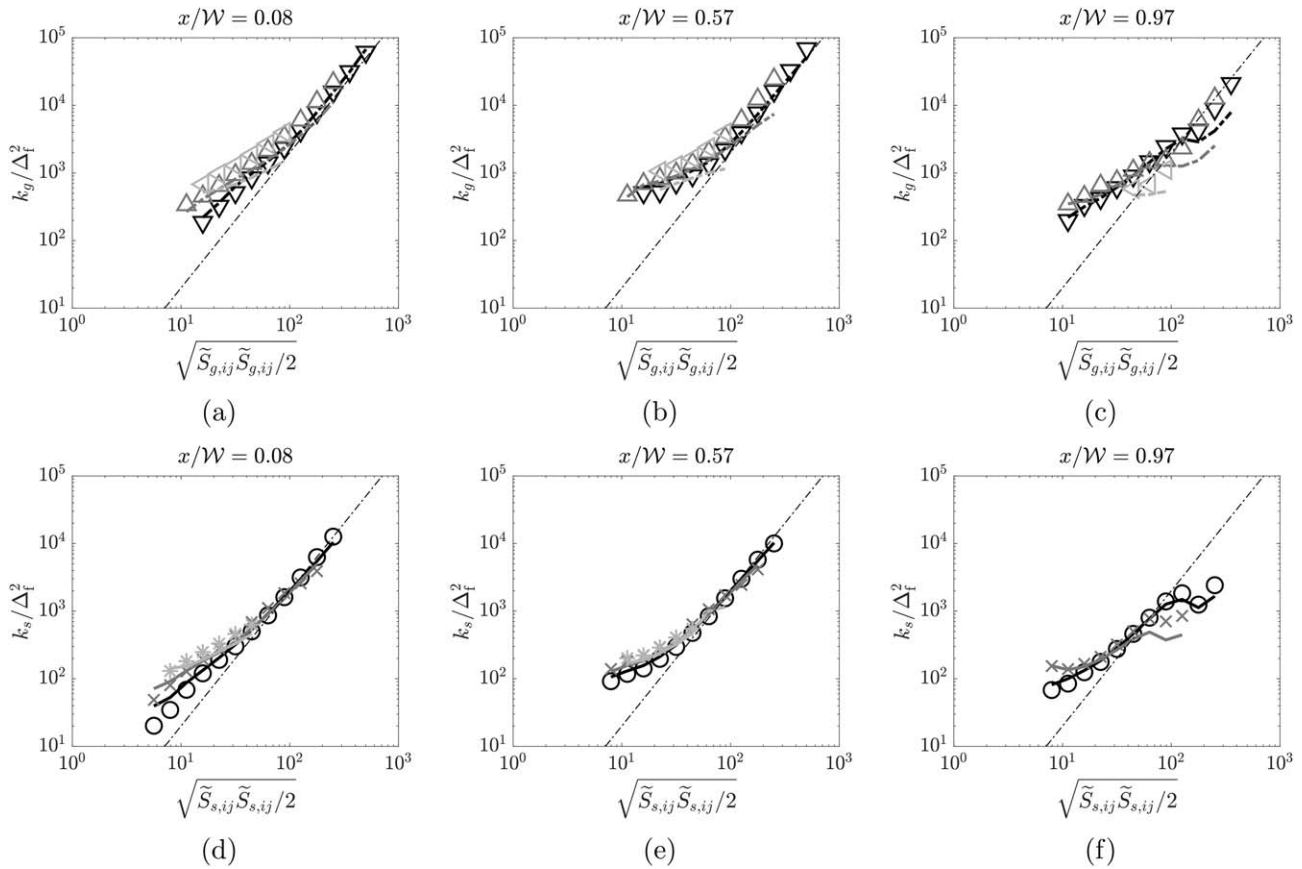


**Figure 11. Normalized large-scale TKEs of the gas and solid phase,  $k_g/\Delta_f^2$  and  $k_s/\Delta_f^2$ , as a function of the scalar shearrates,  $\sqrt{\tilde{S}_{g,ij}\tilde{S}_{g,ij}/2}$  and  $\sqrt{\tilde{S}_{s,ij}\tilde{S}_{s,ij}/2}$ , at different locations  $x/W$  for Case 2.**

The symbols and lines have the same meaning as in Figure 10.

Figures 4a–c further show that Eq. 3 provides fairly good estimates of  $H$  near the bounding walls for different filtered solids volume fractions. Remarkably, it appears that no wall corrections for  $H$  are required here. However, it has to be noted that for the evaluation of  $H(k_g, k_s, \phi^2)$ , the TKEs of the gas and the solid phase ( $k_g$  and  $k_s$ ) as well as of VVF ( $\phi^2$ )

were determined directly from the fine grid simulations (instead of using Eqs. 4 and 6 summarized in Table 1) in order to study the accuracy of Eq. 3 itself. The predictiveness of the constitutive relations for  $k_g$ ,  $k_s$ , and  $\phi^2$  is discussed later. It has to be further stressed that the model constants given in Table 1 take the same values throughout the article and these

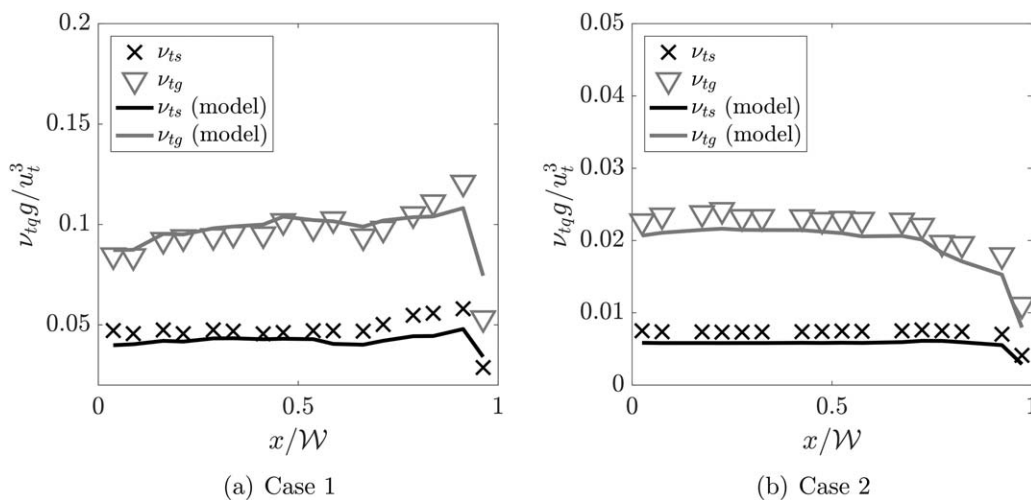


**Figure 12. Normalized large-scale viscosities of the gas and solid phase,  $\nu_{tq}g/u_t^3$  and  $\nu_{ts}g/u_t^3$ , as a function of the normalized horizontal coordinate,  $x/W$ , for  $\Delta_f=7.5$ .**

The symbols correspond to measurements from the fine grid simulations and the solid lines denote the predictions employing Eq. 5 with  $l_{mq} = C_{vq} \min(\Delta_f, \delta)$ .

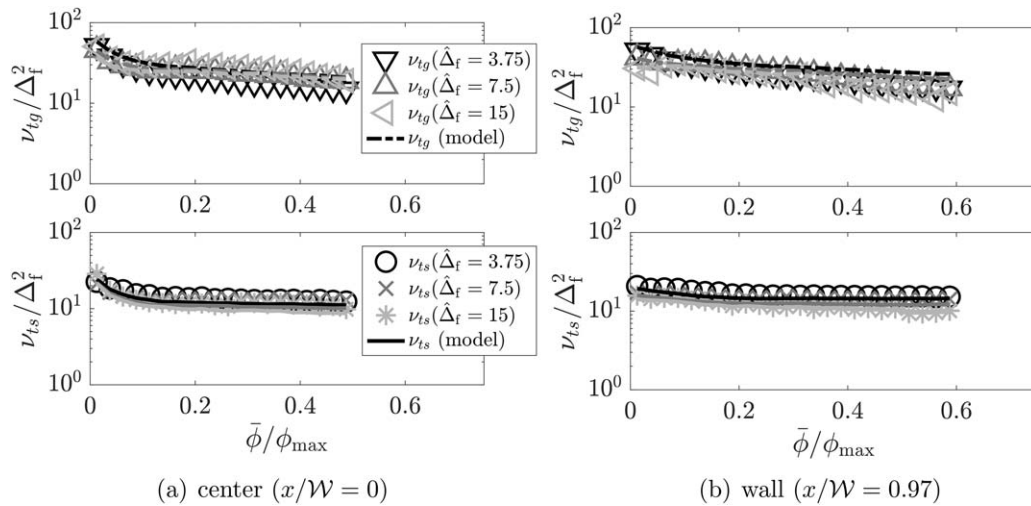


**Figure 13. Normalized kinematic large-scale viscosities of the gas and solid phase,  $\nu_{tg}/\Delta_f^2$  and  $\nu_{ts}g/u_t^3$ , as a function of the normalized filtered solids volume fraction,  $\bar{\phi}/\phi_{\max}$ , for Case 1 in (a) the center of the channel and (b) near the walls.**

The symbols correspond to measurements from the fine grid simulations and the solid lines denote the predictions employing Eq. 5.

are, therefore, not adjusted to improve the agreement between model predictions and filtered data. In addition, Figure 4c shows exemplarily the prediction of the filtered sub-grid drag modification of Sarkar et al.,<sup>27</sup> which employs a two-marker representation, that is  $H(\bar{\phi}, \tilde{u}_{gs})$ ; these are the filtered solids volume fraction and the filtered gas–solid slip velocity. According to Milioli et al.<sup>26</sup> the two-marker representation of the filtered drag force may be appropriate to account for the different sub-filter behavior near walls. However, our results do not support this assumption. While the correlation of Sarkar et al.<sup>27</sup> unveils nearly no reduction of  $H$  for  $x/W < 0.8$  in correspondence with the fine grid data, it does not exhibit a reduction of  $H$  in the annulus region (i.e.,  $x/W > 0.8$ ) as well. The latter can be explained by the merely slight increase of the filtered slip velocity in the annular region (not shown here). Solely a considerable increase of the filtered slip velocity would yield the appropriate behavior of  $H(\bar{\phi}, \tilde{u}_{gs})$  near the

wall. This, in turn implies, that the sub-grid state near the solid walls cannot be characterized appropriately by only using the filtered solids volume fraction and the filtered slip velocity.

As extensively discussed in our previous study,<sup>1</sup> the fractional correction of the drag force  $H$  is considerably affected by the formation of sub-grid clusters (i.e., heterogenous sub-grid structures), which can be reduced to the value of  $\bar{\phi}^2$ . Thus, in Figure 5 the sub-grid drag modification  $H$  is plotted as a function of  $\bar{\phi}^2$  for different locations in the channel,  $x/W$ , for Case 1. Note that  $x/W = 0.97$  is very close to the solid walls. In particular, the distance to the wall is  $4\mathbb{L}_{ch}$ . The figure reveals that Eq. 3 correctly predicts the functional dependency of  $H$  on VVF. Interestingly, in this representation  $H$  does not unveil a considerable filter size dependence. In fact, samples of larger  $\bar{\phi}^2$  correspond to larger filter sizes and these, in turn, show larger values of  $H$ . Remarkably, the Taylor expansion approach yields even good predictions at large

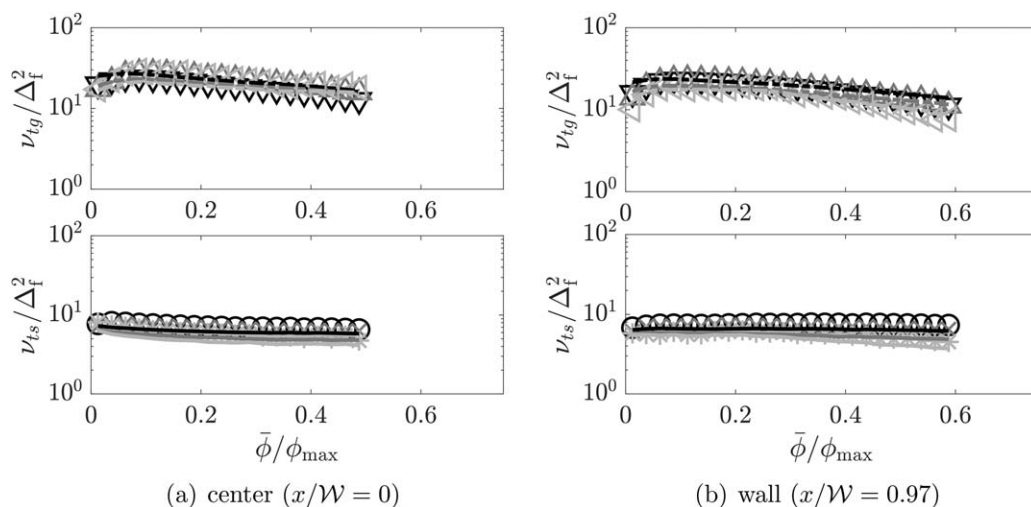


**Figure 14. Normalized kinematic large-scale viscosities of the gas and solid phase,  $\nu_{tg}/\Delta_f^2$ , as a function of the normalized filtered solids volume fraction,  $\bar{\phi}/\phi_{\max}$ , for Case 2 in (a) the center of the channel and (b) near the walls.**

The lines and symbols have the same meaning as in Figure 13.

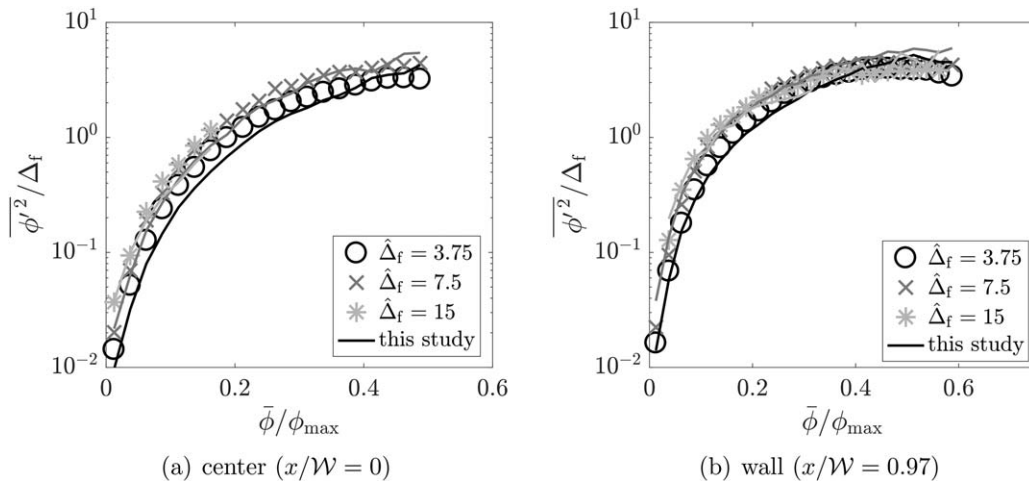


**Figure 15. Normalized variance of the solids volume fraction,  $\overline{\phi'^2}/\Delta_f$ , as a function of the normalized filtered solids volume fraction,  $\bar{\phi}/\phi_{\max}$ , for Case 1 in (a) the center of the channel and (b) near the walls.**

The symbols correspond to measurements from the fine grid simulations and the solid lines denote the predictions employing Eq. 6.

$\overline{\phi'^2}$  in the core of the channel. However, in the annulus, Eq. 3 slightly underpredicts the fine grid data for very large  $\overline{\phi'^2}$ . Here, considering higher order terms in the Taylor expansion of the microscopic drag force  $\beta(\mathbf{v}-\mathbf{u})$  may improve the predictions very close to the wall for  $\overline{\phi'^2}-\bar{\phi}^2$ .<sup>76</sup> Since the error is very small, we do not discuss these higher order approximations in this article. This will be done in future studies.

In Figures 6 and 7 the predictions of Eq. 3 are compared with fine grid data obtained from simulations using Geldart B particles (Case 2). On the one hand, Figure 6 confirms that Eq. 3 yields an appropriate scaling of  $H$  with the particle properties, such as density and diameter. However, it has to be noted that for the Geldart B particles the agreement of Eq. 3 with the fine grid data is not as good as obtained for Case 1. This is stemming from the correlation coefficients (model constants)  $\xi_{\phi_g}$  and  $\xi_{\phi_s}$ , which do not show exactly the same values in both cases; nevertheless, to examine the predictability of the SA-TFM approach, we used the values given in Table 1 for the model constants throughout the article as emphasized earlier. To further improve the SA-TFM-predictions, future

studies will adapt a dynamic adjustment procedure,<sup>28,29,77</sup> which enables the determination of those coefficients directly from the coarse-grid simulation. On the other hand, Figure 6b suggests that near solid boundaries the drag reduction obtained for Case 2 enhances as well. It has to be further delineated that Case 2 shows a core-annular flow similar to Case 1 (compare with Figure 1) with a dilute core and a dense annular flow. In this respect, Figure 7 reveals that for larger particles the influence of the dense annular region is much more pronounced toward the channel center (approx. from  $0.6 < x/W < 1$ ), while in the case of Geldart A particles only a small region near the wall shows a different behavior compared to the core (approx. from  $0.8 < x/W < 1$ ). This can be explained by the integral length scale of the “eddies” of the solids velocity, which is  $u_t^2/g$ .<sup>49</sup> While for Case 2 this integral length is eight times larger than the integrals lengths scale for Case 1, the domain size for Case 2 is just four times larger since we scaled the channel using  $(u_t^2/g)\text{Fr}^{-2/3}$ . Note that the latter length scale corresponds to a dissipation length scale, where the particle clusters dissipate to “molecular” fluctuations.<sup>75</sup> To sum up,

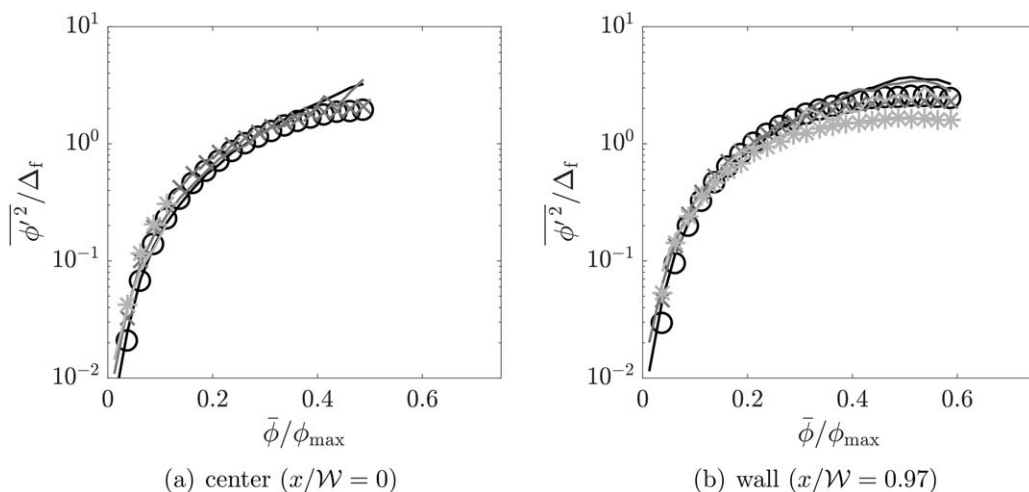


**Figure 16. Normalized variance of the solids volume fraction,  $\overline{\phi'^2}/\Delta_f$ , as a function of the normalized filtered solids volume fraction,  $\bar{\phi}/\phi_{\max}$ , for Case 2 in (a) the center of the channel and (b) near the walls.**

The symbols and lines have the same meaning as in Figure 15.

Eq. 3, in turn, precisely estimates the increase of the drag reduction with decreasing distance from the solid walls. In contrast, the two-marker filter drag modification  $H(\bar{\phi}, \tilde{u}_{gs})$  proposed by Schneiderbauer and Pirker,<sup>20</sup> which was derived from highly resolved bubbling fluidized bed simulations of Geldart B particles, does not appropriately account for the different clustering behavior near the walls, even though a second marker is used to characterize the sub-filter state. In fact, the model of Schneiderbauer and Pirker<sup>20</sup> actually predicts a smaller reduction of the drag force near the walls than in the center (i.e.,  $(1-H)/(1-H_{\text{center}}) > 1$ ) since on average our fine grid simulation of Case 2 unveils smaller filtered slip velocities in the annular region than in the core of the channel (not shown here).

To be able to compute the fractional correction of the resolved drag force  $H$  in a coarse grid simulation, it remains to discuss the constitutive relations for  $k_g$ ,  $k_s$ , and  $\bar{\phi}^2$ . Figure 8a demonstrates that the present constitutive relations for  $k_g$  and  $k_s$  (Eq. 4) considerably overestimate the TKE near the solid walls when employing equation  $l_{mq} = C_{vq} \Delta_f$  (dotted line), where  $q$  denotes either the gas  $g$  or solid phase  $s$ . It is well known from single phase turbulence modeling that such a simple model for the mixing length does not unveil the correct limit of the TKE near the wall.<sup>78</sup> In analogy, to the single phase Smagorinsky model<sup>79</sup> we employ the following correction to  $l_{mq}$

$$l_{mq} = C_{vq} \min(\Delta_f, \delta), \quad (13)$$

where  $\delta$  is the distance from the wall. However, even though employing Eq. 13 considerably improves the estimates of  $k_q$  near the wall, Eq. 4 overpredicts the TKEs in the annular region. This can be explained by the high anisotropy of the components of the TKE near solid walls.<sup>41</sup> While the wall-normal components of solid phase velocity fluctuations tends to zero when approaching the wall, the tangential fluctuations are solely damped by elastic frictional particle-wall collisions. Thus, we employ the following representation for  $k_q$  directly adjacent to solid boundaries

$$\begin{aligned} \tilde{k}_{q,\perp} &= 0, \\ \tilde{k}_{q,\parallel} &= \tilde{k}_q = \frac{2}{3} k_q, \end{aligned} \quad (14)$$

where  $k_q$  is computed from Eq. 4 using Eq. 13. Remarkably, this simple approximation of the anisotropy of the TKE near the wall appropriately predicts the TKE for  $x/\mathcal{W} > 0.9$  for both particle types, i.e., Cases 1 and 2 (solid lines in Figure 8). It has to be further emphasized that the algebraic Eq. 4 appears sufficient to determine the TKEs accurately and thus, it is apparent that the convective and diffusive transport have solely a minor role in moderately dense gas-solid flows.

Figure 8 additionally reveals that the profiles of  $k_q(x)$  strongly depend on the particle properties. While in the case of the Geldart A type particles  $k_q(x)$  show their maximum value very close to the solid walls, in the case of the Geldart B type particles  $k_q(x)$  exhibits a maximum near the core of the channel. The different behavior of the TKEs can be delineated as follows. Similar to turbulent single phase channel flows, high shear rates near the wall generate turbulent velocity fluctuations. However, in gas-solid flows there is a second mechanism generating those turbulent fluctuations, that is the interfacial work. Due to this latter process TKE is transferred from the gas to solid phase, which results in a reduction of  $k_g$  and in an increase of  $k_s$ ; this mechanism appears more pronounced near walls. In addition, as already elaborated the

integral length scale of the turbulent eddies is much larger in the case of the type B particles than in the case of type A particles. This, in turn, implies that the maximum of the TKEs (which is also observed in single phase flows) is closer to the wall in the case of small particles. Finally, it has to be emphasized that the model constant  $C_{eg}$  ( $=0.7$ ) appearing in Eq. 4 takes a slightly smaller value than in our previous work,<sup>1</sup> where it was set to  $C_{eg} = 1$ . This might be related to the considerably higher superficial gas velocities employed in this study, which are at least 10 times higher than in Schneiderbauer.<sup>1</sup> Future studies will elaborate in more detail the dependence of  $C_{eg}$  on  $W_g$ .

To investigate the variation of the bin-averaged model predictions, Figure 9 exemplarily presents a parity plot comparing the model predictions for the solid-phase TKE (Eq. 4) with their filtered counterparts obtained from the fine grid simulation of Case 1. The figure clearly shows that most of the data points are very close to the identity line indicating a good agreement between Eq. 4 and the filtered solid-phase TKE. It has to be stressed that pairs of measured (from fine grid simulation) and modeled TKEs far away from the identity line are very unlikely to occur. Furthermore, computing the Pearson correlation coefficient,  $\rho$ , unveils a high positive correlation between filtered and modeled TKEs. In particular, we find  $\rho > 0.8$  for both, the gas and the solid phase.

As elucidated in the previous paragraphs, in gas-solid flows there are two main production mechanisms generating turbulent velocity fluctuations. The production due to gradients of the velocity (shear induced turbulence, SIT) is dominant in regions of high shear rates; here,  $k_q \propto \tilde{S}_{q,ij} \tilde{S}_{q,ij}$  ( $q \in \{g, s\}$ ), which is also indicated by the dashed-dotted lines in Figures 10 and 11. In contrast, the production due to interfacial work (CIT) is important in regions of low shear rates. In this case, where  $\sqrt{\tilde{S}_{q,ij} \tilde{S}_{q,ij}}/2 \lesssim 10^2$ , Figures 10 and 11 reveal that  $k_q$  is determined by the contribution stemming from the interfacial work, which is considerably larger than the contribution coming from SIT (dashed-dotted line in Figures 10 and 11). It has to be emphasized that the contribution of CIT is effective as long as the slip velocity is non-zero (i.e., the drag coefficient is non-zero), even though there is no meso-scopic shear.<sup>1,40-43</sup> Figures 10 and 11 further demonstrate that Eq. 11 is in fairly good agreement with the numerical data obtained from highly resolved simulations. Especially close to solid walls, again the considerable reduction of the TKEs is observed for the Geldart B type particles.

In our previous study, we demonstrated that the micro-scale turbulent kinematic viscosity,  $\nu_{tq}$ , can be closed by employing a mixing length assumption (compare with Eq. 5). Thus, the shear viscosity resulting from the enhanced diffusion due to the turbulent velocity fluctuations is directly connected to the TKE, that is  $\nu_{tq} = l_{mq} k_q^{1/2}$ . In Figure 12 the normalized turbulent kinematic viscosity is plotted as a function of the normalized horizontal coordinate,  $x/\mathcal{W}$ , for Geldart type A and B particles. As demonstrated earlier the presence of solid boundaries is much more distinct for the type B particles due to the larger cluster sizes. Close to the wall,  $\nu_{tq} = l_{mq} k_q^{1/2}$  vanishes due to the damping of the wall-normal velocity fluctuations. However, in contrast to single phase flows  $\nu_{tq}$  does not tend to zero as  $\delta$  approaches zero, since the wall-tangential velocity fluctuations are generally non-zero.<sup>41,42</sup> Even though, we employ a very simple isotropic closure for the turbulent viscosities of both, the gas and the solid phase, our model predictions

correlate well with the highly resolved simulations. Additionally, Figures 13 and 14 show the turbulent kinematic viscosities as a function of the solids volume fraction in the core of the channel and near the solid boundaries. As already delineated in our previous study,<sup>1</sup>  $\nu_{tq}$  and  $k_q$  (Figures 10 and 11) scale with the square of the filter size, which is in accordance to single phase turbulence. Generally, the kinematic viscosity appears to be higher at low to intermediate volume fractions and tends to zero as the volume fraction approaches maximum packing conditions. The latter is evident, since at maximum packing there is simply no room for turbulent fluctuations. For a more detailed discussion on the specific features of  $\nu_{tq}$  and  $k_q$  the reader is referred to Schneiderbauer.<sup>1</sup>

Finally, we have to discuss the variance of the filtered solids volume fraction (VVF). Figures 15 and 16 show the VVF as a function of the solids volume fraction in the core of the channel as well as near the solid boundaries for Geldart type A and type B particles. The figures unveil that the fluctuations of the solids volume fraction do not show a considerable dependence on the horizontal position,  $x/W$ , in the channel. In particular,  $\overline{\phi'^2}$  shows only a minor enlargement when approaching the wall. It is, therefore, concluded that the increase of the drag reduction detected in the vicinity of the solid boundaries is mainly coming from the TKEs, since  $H \propto \sqrt{\overline{\phi'^2}} (\xi_{\phi_g} \sqrt{k_g} - \xi_{\phi_s} \sqrt{k_s})$  (compare with Eq. 3). However, the magnitude of the correlation coefficient  $\xi_{\phi_g}$  appears to be much larger than  $\xi_{\phi_s}$ , which is nearly zero (compare with Table 1). This, in turn, implies that the additional drag reduction in the vicinity near wall is mainly stemming from the gas-phase TKE, which is particularly evident for the Geldart type A particles (Figure 8a). It has to be further highlighted that Eq. 6 is fairly consistent with the data stemming from the highly resolved simulations.

In summary, we are able to draw the following picture of turbulent structures in moderately dense gas–solid flow.<sup>44</sup> Meso-scale shear and drag generate eddies of the gas and solids velocity with the size of approximately  $u_t^2/g$ . These eddies break up to smaller eddies; together with gradients in the solids volume fraction those smaller eddies trigger particle clusters (Eq. 6), which are generally smaller than the large eddies. Clusters and eddies further break up and transfer their energy successively to smaller clusters and eddies until inter-particle collisions get dominant at  $(u_t^2/g)Fr^{-2/3}$ .<sup>75</sup> Here, these clusters and eddies dissipate their TKE, which is consequently converted into “molecular” fluctuations. The latter are characterized by the granular temperature.

## Conclusions and Outlook

In this article, we have verified the constitutive relation for the unresolved terms appearing in the SA-TFM model in the vicinity of solid boundaries. Thereby, we employed an *a priori* analysis by comparing the predictions of these constitutive relations with highly resolved simulations of gas–solid channel flows. The main findings are

1. Consistent with previous work,<sup>23</sup> we observe a considerable increase of the drag reduction in the vicinity of solid boundaries. Employing an averaged (filtered) linearized micro-scopic drag force appears sufficient to capture this different cluster behavior near walls.

2. The TKEs and the turbulent viscosities are strongly affected by the presence of the solid boundaries. While in the channel core the algebraic constitutive relations for the TKEs and the turbulent viscosities yield fairly good agreement with

the highly resolved simulations, in the vicinity of the walls the mixing length has to be adapted according to Smagorinsky sub-grid scale model,<sup>79</sup> i.e.,  $l_{mq} = C_{vq} \min(\Delta_f, \delta)$ .

3. The components of the fluctuation velocity are highly anisotropic near the wall, since the wall-normal components of solid phase velocity fluctuations tend to zero, while the wall-tangential components of solid phase velocity fluctuations solely experience a damping due to particle-wall collisions. Thus, in a coarse grid simulations this has to be accounted for by setting the meso-scale pressure at the wall to zero in wall-normal direction.

To sum up, the presented constitutive relations for the unresolved terms appearing in the SA-TFM approach are in fairly good agreement with highly resolved simulations of wall dominated channel flows. Future work should first concentrate on withdrawing the assumption of isotropic turbulence. In contrast, the current constitutive relation should be generalized to account for anisotropic conditions. Second, the applicability of the SA-TFM approach in the case of dilute gas–particle flows should be studied. Third, the simplifying assumptions of the SA-TFM approach (i.e., dropping the filtered kinetic theory stresses and the local-equilibrium hypothesis of the TKEs) should be investigated more thoroughly. Especially, the impact of the filtered kinetic theory stresses in a transient state will be studied. Finally, the present model has not been validated against experimental data. The latter will be done in Part II<sup>50</sup> of this article.

## Acknowledgments

This work was funded by the Christian-Doppler Research Association, the Austrian Federal Ministry of Economy, Family and Youth, and the Austrian National Foundation for Research, Technology and Development. The author also wants to acknowledge the financial support from the KIMET center for metallurgical research in Austria (www.k1-met.com).

## Literature Cited

- Schneiderbauer S. A spatially-averaged two-fluid model for dense large-scale gas-solid flows. *AIChE J.* 2017;63(8):3544–3562.
- Agrawal K, Loezos PN, Syamlal M, Sundaresan S. The role of meso-scale structures in rapid gas-solid flows. *J Fluid Mech.* 2001; 445:151–185.
- Chevrier S. Development of sub-grid models for a periodic circulating fluidized bed of binary mixture of particles. PhD thesis, University of Toulouse. 2017.
- Chew JW, Hays R, Findlay JG, Knowlton TM, Reddy Karri SB, Cocco RA, Hrenya CM. Cluster characteristics of Geldart Group B particles in a pilot-scale CFB riser. I. Monodisperse systems. *Chem Eng Sci.* 2012;68(1):72–81.
- Sharma AK, Tuzla K, Matsen J, Chen JC. Parametric effects of particle size and gas velocity on cluster characteristics in fast fluidized beds. *Powder Technol.* 2000;111(1–2):114–122.
- Harris AT, Davidson JF, Thorpe RB. The prediction of particle cluster properties in the near wall region of a vertical riser (200157). *Powder Technol.* 2002;127(2):128–143.
- Glasser B, Sundaresan S, Kevrekidis I. From bubbles to clusters in fluidized beds. *Phys Rev Lett.* 1998;81(9):1849–1852.
- Zou B, Li H, Xia Y, Ma X. Cluster structure in a circulating fluidized bed. *Powder Technol.* 1994;78(2):173–178.
- Schneiderbauer S, Aigner A, Pirker S. A comprehensive frictional-kinetic model for gas-particle flows: analysis of fluidized and moving bed regimes. *Chem Eng Sci.* 2012;80:279–292.
- Li J, Kwauk M. *Particle-Fluid Two-Phase Flow: The Energy-Minimization Multi-Scale Method.* Beijing: Metallurgical Industry Press, 1994.

11. Liu M, Li J, Kwauk M. Application of the energy-minimization multi-scale method to gas-liquid-solid fluidized beds. *Chem Eng Sci.* 2001;56(24):6805–6812.
12. Lu B, Wang W, Li J. Searching for a mesh-independent sub-grid model for CFD simulation of gas-solid riser flows. *Chem Eng Sci.* 2009;64(15):3437–3447.
13. Hong K, Wang W, Zhou Q, Wang J, Li J. An EMMS-based multi-fluid model (EFM) for heterogeneous gas-solid riser flows: part I. Formulation of structure-dependent conservation equations. *Chem Eng Sci.* 2012;75:376–389.
14. Schneiderbauer S, Pirker S. A coarse-grained two-fluid model for gas-solid fluidized beds. *J Comput Multiphase Flows.* 2014;6(1):29–47.
15. Schneiderbauer S, Puttinger S, Pirker S, Aguayo P, Kanellopoulos V. CFD modeling and simulation of industrial scale olefin polymerization fluidized bed reactors. *Chem Eng J.* 2015;264:99–112.
16. Schneiderbauer S, Puttinger S, Pirker S. Comparative analysis of subgrid drag modifications for dense gas-particle flows in bubbling fluidized beds. *AIChE J.* 2013;59(11):4077–4099.
17. Huilin L, Qiaoqun S, Yurong H, Yongli S, Ding J, Xiang L. Numerical study of particle cluster flow in risers with cluster-based approach. *Chem Eng Sci.* 2005;60(23):6757–6767.
18. Hong K, Chen S, Wang W, Li J. Fine-grid two-fluid modeling of fluidization of Geldart A particles. *Powder Technol.* 2016;296:2–16.
19. Luo H, Lu B, Zhang J, Wu H, Wang W. A grid-independent EMMS/bubbling drag model for bubbling and turbulent fluidization. *Chem Eng J.* 2017;326:47–57.
20. Schneiderbauer S, Pirker S. Filtered and heterogeneity based sub-grid modifications for gas-solid drag and solids stresses in bubbling fluidized beds. *AIChE J.* 2014;60(3):839–854.
21. Wang J, Ge W, Li J. Eulerian simulation of heterogeneous gas-solid flows in CFB risers: EMMS-based sub-grid scale model with a revised cluster description. *Chem Eng Sci.* 2008;63(6):1553–1571.
22. Igci Y, Andrews AT, Sundaresan S, Pannala S, O'Brien T. Filtered two-fluid models for fluidized gas-particle suspensions. *AIChE J.* 2008;54(6):1431–1448.
23. Igci Y, Sundaresan S. Constitutive models for filtered two-fluid models of fluidized gas-particle flows. *Ind Eng Chem Res.* 2011;50(23):13190–13201.
24. Igci Y, Sundaresan S. Verification of filtered two-fluid models for gas-particle flows in risers. *AIChE J.* 2011;57(10):2691–2707.
25. Igci Y, Pannala S, Benyahia S, Sundaresan S. Validation studies on filtered model equations for gas-particle flows in risers. *Ind Eng Chem Res.* 2012;51(4):2094–2103.
26. Milioli CC, Milioli FE, Holloway W, Agrawal K, Sundaresan S. Filtered two-fluid models of fluidized gas-particle flows: new constitutive relations. *AIChE J.* 2013;59(9):3265–3275.
27. Sarkar A, Milioli FE, Ozarkar SS, Li T, Sun X, Sundaresan S. Filtered sub-grid constitutive models for fluidized gas-particle flows constructed from 3-D simulations. *Chem Eng Sci.* 2016;152:443–456.
28. Parmentier JF, Simonin O, Delsart O. A functional subgrid drift velocity model for filtered drag prediction in dense fluidized bed. *AIChE J.* 2012;58(4):1084–1098.
29. Ozel A, Fede P, Simonin O. Development of filtered Euler-Euler two-phase model for circulating fluidised bed: High resolution simulation, formulation and a priori analyses. *Int J Multiphase Flow.* 2013;55:43–63.
30. Cloete JH, Cloete S, Municchi F, Radl S, Amini S. The sensitivity of filtered two fluid models to the underlying resolved simulation setup. *Powder Technol.* 2017;316:265–277.
31. Sarkar A, Sun X, Sundaresan S. Sub-grid drag models for horizontal cylinder arrays immersed in gas-particle multiphase flows. *Chem Eng Sci.* 2013;104:399–412.
32. Shah S, Ritvanen J, Hyppänen T, Kallio S. Space averaging on a gas-solid drag model for numerical simulations of a CFB riser. *Powder Technol.* 2012;218:131–139.
33. Holloway W, Sundaresan S. Filtered models for reacting gas-particle flows. *Chem Eng Sci.* 2012;82:132–143.
34. Holloway W, Sundaresan S. Filtered models for bidisperse gas-particle flows. *Chem Eng Sci.* 2014;108:67–86.
35. Ozel A, Kolehmainen J, Radl S, Sundaresan S. Fluid and particle coarsening of drag force for discrete-parcel approach. *Chem Eng Sci.* 2016;155:258–267.
36. Ozel A, Gu Y, Milioli CC, Kolehmainen J, Sundaresan S. Towards filtered drag force model for non-cohesive and cohesive particle-gas flows. *Phys Fluid.* 2017;29(10):103308.
37. Radl S, Sundaresan S. A drag model for filtered Euler-Lagrange simulations of clustered gas-particle suspensions. *Chem Eng Sci.* 2014;117:416–425.
38. Zhu LT, Xie L, Xiao J, Luo ZH. Filtered model for the cold-model gas-solid flow in a large-scale MTO fluidized bed reactor. *Chem Eng Sci.* 2016;143:369–383.
39. Cloete S, Johansen ST, Amini S. Evaluation of a filtered model for the simulation of large scale bubbling and turbulent fluidized beds. *Powder Technol.* 2013;235:91–102.
40. Fox RO. On multiphase turbulence models for collisional fluid-particle flows. *J Fluid Mech.* 2014;742:368–424.
41. Capecelatro J, Desjardins O, Fox RO. Strongly coupled fluid-particle flows in vertical channels. II. Turbulence modeling. *Phys Fluid.* 2016;28(3):033307.
42. Capecelatro J, Desjardins O, Fox RO. Strongly coupled fluid-particle flows in vertical channels. I. Reynolds-averaged two-phase turbulence statistics. *Phys Fluid.* 2016;28(3):033306.
43. Capecelatro J, Desjardins O, Fox RO. On fluid-particle dynamics in fully developed cluster-induced turbulence. *J Fluid Mech.* 2015;780:578–635.
44. Schneiderbauer S, Saeedipour M. Approximate deconvolution model for the simulation of turbulent gas-solid flows: an a-priori analysis. *Phys Fluid.* 2018;30(2):023301.
45. Hrenya CM, Sinclair JL. Effects of particle-phase turbulence in gas-solid flows. *AIChE J.* 1997;43(4):853–869.
46. Benavides A, van Wachem BGM. Numerical simulation and validation of dilute turbulent gas-particle flow with inelastic collisions and turbulence modulation. *Powder Technol.* 2008;182(2):294–306.
47. Rao A, Curtis JS, Hancock BC, Wassgren C. Numerical simulation of dilute turbulent gas-particle flow with turbulence modulation. *AIChE J.* 2012;58(5):1381–1396.
48. Simonin O. Continuum modeling of dispersed two-phase flows, combustion and turbulence in two-phase flows. In: *Lecture Series—Von Karman Institute of Fluid Dynamics*, pp. 1–47. Van Karem Institute, 1996.
49. Capecelatro J, Desjardins O, Fox RO. Numerical study of collisional particle dynamics in cluster-induced turbulence. *J Fluid Mech.* 2014;747:R2.
50. Schneiderbauer S. Validation study on spatially averaged two-fluid model for gas-solid flows. II: Application to risers and bubbling fluidized beds. *AIChE J.* 2017. doi: 10.1002/aic.16141.
51. Zhu H. Turbulent fluidized bed vs. high density riser—regimes and flow characterizations. PhD thesis, The University of Western Ontario, 2006.
52. Zhu H, Zhu J, Li G, Li F. Detailed measurements of flow structure inside a dense gas-solids fluidized bed. *Powder Technol.* 2008;180(3):339–349.
53. Panday R, Shadle LJ, Shahnam M, Cocco R, Issangya A, Spenik JS, Ludlow JC, Gopalan B, Shaffer F, Syamlal M, Guenther C, Reddy Karri SB, Knowlton T. Challenge problem: 1. Model validation of circulating fluidized beds. *Powder Technol.* 2014;258:370–391.
54. O'Brien TJ. A multiphase turbulence theory for gassolid flows: I. Continuity and momentum equations with Favre-averaging. *Powder Technol.* 2014;265:83–87.
55. Jiménez C, Ducros F, Cuenot B, Bédat B. Subgrid scale variance and dissipation of a scalar field in large eddy simulations. *Phys Fluid.* 2001;13(6):1748–1754.
56. Lun CKK, Savage SB, Jeffrey DJ, Chepurmy N. Kinetic theories for granular flow: inelastic particles in Couette flow and slightly inelastic particles in a general flowfield. *J Fluid Mech.* 1984;140(1):223–256.
57. Chialvo S, Sun J, Sundaresan S. Bridging the rheology of granular flows in three regimes. *Phys Rev E.* 2012;85(2 Pt 1):021305.
58. Schneiderbauer S, Schellander D, Löderer A, Pirker S. Non-steady state boundary conditions for collisional granular flows at flat frictional moving walls. *Int J Multiphase Flow.* 2012;43:149–156.
59. Jenkins JT. Boundary conditions for rapid granular flows: flat, frictional walls. *J Appl Mech.* 1992;59(1):120–127.
60. Louge MY. Computer simulations of rapid granular flows of spheres interacting with a flat, frictional boundary. *Phys Fluid.* 1994;6(7):2253–2269.
61. Jenkins JT, Louge MY. On the flux of fluctuation energy in a collisional grain flow at a flat, frictional wall. *Phys Fluid.* 1997;9(10):2835–2840.
62. Nasuno S, Kudrolli A, Bak A, Gollub JP. Time-resolved studies of stick-slip friction in sheared granular layers. *Phys Rev E.* 1998;58(2):2161.

63. Sommerfeld M, Huber N. Experimental analysis and modelling of particle-wall collisions. *Int J Multiphase Flow*. 1999;25(6-7):1457-1489.
64. Baldassarri A, Dalton F, Petri A, Zapperi S, Pontuale G, Pietronero L. Brownian forces in sheared granular matter. *Phys Rev Lett*. 2006;96(11):1-4.
65. Artoni R, Santomaso A, Canu P. Effective boundary conditions for dense granular flows. *Phys Rev E*. 2009;79(3):031304.
66. Cloete JH, Cloete S, Radl S, Amini S. Evaluation of wall friction models for riser flow. *Powder Technol*. 2016;303:156-167.
67. Fullmer WD, Hrenya CM. Quantitative assessment of fine-grid kinetic-theory-based predictions of mean-slip in unbounded fluidization. *AIChE J*. 2016;61(1):11-17.
68. Fullmer WD, Hrenya CM. The clustering instability in rapid granular and gas-solid flows granular medium: solid particles in the absence of an interstitial (carrier) phase or in the presence of a negligible gas phase. *Annu Rev Fluid Mech*. 2017;49:485-510.
69. Uddin MH, Coronella CJ. Grid effect on bed expansion of bubbling fluidized beds of Geldart B particles: a generalized rule for a grid independent solution for TFM simulations. *Particuology*. 2017;34:61-69.
70. Wang J, van der Hoef MA, Kuipers JAM. Why the two-fluid model fails to predict the bed expansion characteristics of Geldart A particles in gas-fluidized beds: A tentative answer. *Chem Eng Sci*. 2009;64(3):622-625.
71. Li T, Grace J, Bi X. Study of wall boundary condition in numerical simulations of bubbling fluidized beds. *Powder Technology*. 2010;203(3):447-457.
72. Andrews AT, Loezos PN, Sundaresan S. Coarse-grid simulation of gas-particle flows in vertical risers. *Ind & Eng Chem Res*. 2005;44(16):6022-6037.
73. Benyahia S, Sundaresan S. Do we need sub-grid scale corrections for both continuum and discrete gas-particle flow models? *Powder Technol*. 2012;220:2-6.
74. Benyahia S. Fine-grid simulations of gas-solids flow in a circulating fluidized bed. *AIChE J*. 2012;58(11):3589-3592.
75. Sundaresan S, Radl S, Milioli CC, Milioli FE. Coarse-grained models for momentum, energy and species transport in gas-particle flows. In: *The 14th International Conference on Fluidization—From Fundamentals to Products*, edited by ECI Symposium Series, 2013. Noordwijkerhout, The Netherlands: Engineering Conferences International, NY. 2013:8.
76. Benyahia S. A time-averaged model for gas-solids flow in a one-dimensional vertical channel. *Chem Eng Sci*. 2008;63(9):2536-2547.
77. Germano M, Piomelli U, Moin P, Cabot WH. A dynamic subgrid-scale eddy viscosity model. *Phys Fluid A*. 1991;3(7):1760-1765.
78. Davidson L, Peng SH. Embedded large-eddy simulation using the partially averaged NavierStokes model. *AIAA J*. 2013;51(5):1066-1079.
79. Smagorinsky J. General circulation experiments with the primitive equations. *Month Weather Rev*. 1963;91(3):99-164.

*Manuscript received Nov. 7, 2017, and revision received Feb. 2, 2018.*